Nanoscale

ROYAL SOCIETY OF CHEMISTRY

PAPER

View Article Online
View Journal | View Issue

Cite this: *Nanoscale*, 2024, **16**, 4082

Multiparametric modulation of magnetic transduction for biomolecular sensing in liquids†

Elena Sanz-de Diego,[a] Antonio Aires,[b] Pablo Palacios-Alonso,[a] David Cabrera,[a,c] Niccolo Silvestri,[d] Cinthia C. Vequi-Suplicy,[a] Emilio J. Artés-Ibáñez,[a,e] José Requejo-Isidro,[f,g] Rafael Delgado-Buscalioni,[h] Teresa Pellegrino,[d] Aitziber L. Cortajarena *[a,b,i] and Francisco J. Terán *[a,g]

Received 19th December 2023,
Accepted 24th January 2024

DOI: 10.1039/d3nr06489a

rsc.li/nanoscale

The recent COVID19 pandemic has remarkably boosted the research on *in vitro* diagnosis assays to detect biomarkers in biological fluids. Specificity and sensitivity are mandatory for diagnostic kits aiming to reach clinical stages. Whilst the modulation of sensitivity can significantly improve the detection of biomarkers in liquids, this has been scarcely explored. Here, we report on the proof of concept and parametrization of a novel biosensing methodology based on the changes of AC magnetic hysteresis areas observed for magnetic nanoparticles following biomolecular recognition in liquids. Several parameters are shown to significantly modulate the transducing capacity of magnetic nanoparticles to detect analytes dispersed in saline buffer at concentrations of clinical relevance. Magnetic nanoparticles were bio-conjugated with an engineered recognition peptide as a receptor. Analytes are engineered tetratricopeptide binding domains fused to the fluorescent protein whose dimerization state allows mono- or divalent variants. Our results unveil that the number of receptors per particle, analyte valency and concentration, nanoparticle composition and concentration, and field conditions play a key role in the formation of assemblies driven by biomolecular recognition. Consequently, all these parameters modulate the nanoparticle transduction capacity. Our study provides essential insights into the potential of AC magnetometry for customizing biomarker detection in liquids.

Introduction

The COVID19 pandemic has triggered the research on nanotechnology[1] to achieve user-friendly, quick, and accurate *in vitro* diagnosis assays for the detection of analytes (*i.e.*, biomarkers, antigens, or pathogens) linked to physiological or pathogenic states.[2] Specificity and sensitivity are mandatory features to be accomplished by *in vitro* diagnostic tests aiming to reach clinical use.[3] While specificity is exclusively linked to biological elements denominated receptors, which are involved in the biomolecular recognition of analytes, sensitivity is associated with the receptor–analyte affinity and the transduction element employed to label the receptor–analyte recognition. Generally, the capacity to modulate the detection sensitivity on current sensing methodologies is rather limited, and generally associated with the signal/noise ratio of physical measurements displayed by a transducer. Interestingly, transduction methodologies capable of supplying multiparametric sensitivity gain in versatility for adequate biomarker detection in liquids under experimental circumstances (*i.e.*, biomarker concentration).[4] Recent progress in nanoscience and nanotechnology offers novel transducing potential, such as photoelectrochemical,[5,6] optical,[7,8] colorimetric,[9–11] photothermal,[12] or magnetic[13,14] signal-based methods. Indeed, nanoscale transducers have attracted great attention thanks to their ability to detect biomarkers in biological fluids at concentrations of clinical relevance.[15,16] In general, the physical fundamentals of nanoparticle transduction benefits from its final colloidal state. While the number of reported methodologies[7,8] involving individual nanoparticles to display analyte reco-

[a]*iMdea Nanociencia, Ciudad Universitaria de Cantoblanco, 28049 Madrid, Spain. E-mail: francisco.teran@imdea.org*
[b]*CIC biomaGUNE, Basque Research and Technology Alliance (BRTA), Paseo de Miramón 194, 20014 Donostia-San Sebastián, Spain. E-mail: alcortajarena@cicbiomagune.es*
[c]*School of Pharmacy and Bioengineering, Keele University, Guy Hilton Research Centre, Thurnburrow Drive, ST4 7QB Stoke on Trent, UK*
[d]*Istituto Italiano di Tecnologia, Via Morego 30, 16163 Genoa, Italy*
[e]*Nanotech Solutions, 40150 Villacastín, Spain*
[f]*Centro Nacional de Biotecnologia (CSIC), 28049 Madrid, Spain*
[g]*Nanobiotecnología (iMdea-Nanociencia), Unidad Asociada al Centro Nacional de Biotecnología (CSIC), 28049 Madrid, Spain*
[h]*Dpto Física Teórica Materia Condensada, Universidad Autónoma de Madrid, 28049 Madrid, Spain*
[i]*Ikerbasque, Basque Foundation for Science, Bilbao, Spain*

† Electronic supplementary information (ESI) available. See DOI: https://doi.org/10.1039/d3nr06489a

gnition phenomena is limited, many others take advantage of nanoparticle aggregation.[9,10,12,17–22] More research is needed on detection methodologies based on nanoparticles, whose sensitivity can be tuned by multiple parameters. This is the case for magnetic nanoparticles (MNPs),[23] which have shown great potential as sensing transducers.[14,24] Different experimental techniques[20,22,25–29] such as magnetoresistance, AC magnetic susceptometry, magnetic particle spectroscopy, or relaxivity display changes of MNP magnetic properties after specific interactions with analytes. Such magnetic changes are understood in terms of alterations of the MNP magnetic relaxation processes upon biomolecular recognition.[30,31] Biosensing methodologies are generally required to avoid signal attenuation when operating in biological fluids.[32] This is the case for optical or colorimetric methods, which regularly requires sample purification procedures and operates in limited spectral ranges[33,34] to not interfere with the displayed optical signal (*i.e.* emission, reflection, and absorption). In contrast, magnetic methods have the potential to detect and quantify biomolecules directly in biological samples[35] without requiring further purification procedures. This simplification of sample processing represents a remarkable advantage relying on the magnetic field penetration[36] in biological fluids, which, due to their diamagnetic nature, weakly interact with magnetic fields. Indeed, many reported examples[21,22,25–29,37] of magnetic sensing methodologies found effective transduction when nanoparticles agglomerate due to cross-linking between multiple bio-conjugated MNPs (b-MNPs) and target molecules. Such MNP and analyte agglomerates result in nano-clusters with hydrodynamic sizes (D_H) larger than those of individual MNPs.[22,25,26,28] Such MNP clustering leads to an increase of D_H[38] and intra-aggregate dipolar magnetic interactions,[39,40] which strongly influence the dynamic magnetization cycles. Alternatively, AC magnetometry (ACM) is a versatile and accurate technique employed for characterizing the influence of distinct intrinsic[39] and extrinsic[41–43] parameters on dynamic magnetization and magnetic losses of MNPs dispersed in liquid media or inside cells.[43] Recent works[39] have shown the potential of this technique to directly probe MNP aggregation effects resulting from unspecific interactions between proteins and MNPs. Interestingly, ACM takes advantage of short acquisition times (few seconds) and reduced sample volumes (tens of microlitres) to adequately probe biomolecular recognition dynamics while operating in a wide range of field conditions.[44] Moreover, ACM requires simple operational procedures and minimal sample preparation for probing the presence of biomarkers in biological fluids.[45]

Here, we report on the proof of concept and parametrization of a novel biosensing methodology based on variations of AC magnetic hysteresis areas measured in b-MNPs upon biomolecular recognition in liquids. We assessed the role of various parameters in modulating the changes of colloidal and AC magnetization properties of the resulting b-MNP assemblies. Namely, MNP and analyte concentrations, the number of receptors per MNP, and the analyte valency. Moreover, we evaluated how the nature of MNP magnetic relaxation mechanisms is extremely relevant to transduce biomolecular recognition between receptors and analytes. In addition, the biomolecular recognition in liquids triggers distinct assembly phenomena, resulting in nano-assemblies or nano-clusters depending on the analyte valency. Overall, the above-mentioned parameters strongly influence the colloidal and AC magnetic properties, which modulate the analyte detection sensitivity and allow its customization. Part of our experimental findings were supported by numerical simulations to describe the AC magnetization cycles of individual b-MNPs specifically interacting with multiple analytes and forming nano-assemblies.

Results and discussion

Experimental design of the proposed detection methodology

We employed magnetite and cobalt ferrite MNPs to bio-conjugate an engineered protein that acts as a specific receptor for the analyte (see Fig. 1). The receptor is a designed peptide fused with a final MEEVF sequence to the glutathione *S*-transferase (GST) protein, resulting in GST-MEEVF (see the Experimental section/Methods).[46] Table 1 lists the MNPs employed in this work for trapping mono- or divalent analytes. MNPs were conjugated to display the same average number of receptors on the MNP surface (around 20 receptors per b-MNP). According to the transmission electron microscopy (TEM) and dynamic light scattering (DLS) data, b-MNPs are found to be individually dispersed in 0.1× phosphate buffer (PB), where analytes preserve their structure and recognition capability. In order to study the effects of valency effects, we have chosen analyte monomeric or dimeric Verde fluorescent protein (VFP) variants fused to the peptide-binding tetratricopeptide (TPR) domain (TPR2-MMY, which specifically interacts with the MEEVF peptide).[47] Protein engineering allows the generation of mono- ($VFP_{monomer}$-TPR2-MMY) or divalent (VFP_{dimer}-TPR2-MMY) TPR recognition molecules acting as analytes to specifically interact with the bio-conjugated GST-MEEVF receptor. After incubation of monomeric or dimeric VFP variants with b-MNPs in 0.1× PB (see Experimental section/Methods), biomolecular recognition results in different assemblies (see Fig. 1). For monomer VFPs, nano-assemblies are formed between individual b-MNPs surrounded by multiple analytes specifically bound to the conjugated receptors. The analytes bound to b-MNP lead to surface modifications that strongly influence its translational diffusion. In the case of dimer VFPs, nano-clusters are formed after crosslinking between multiple b-MNPs and analytes, resulting in agglomerates whose D_H are larger than those of individual b-MNPs. The resulting b-MNP and analyte assembly formation leads to an increase of magnetic dipolar interactions, D_H and MNP diffusion values, which strongly influence the magnetic relaxation process.[39,48–50] Consequently, changes of AC magnetization cycles upon biomolecular recognition are expected to provide clear fingerprints of analyte detection in liquids (see Fig. 1). Such transduction signal reflected in AC magnetization changes has been probed by

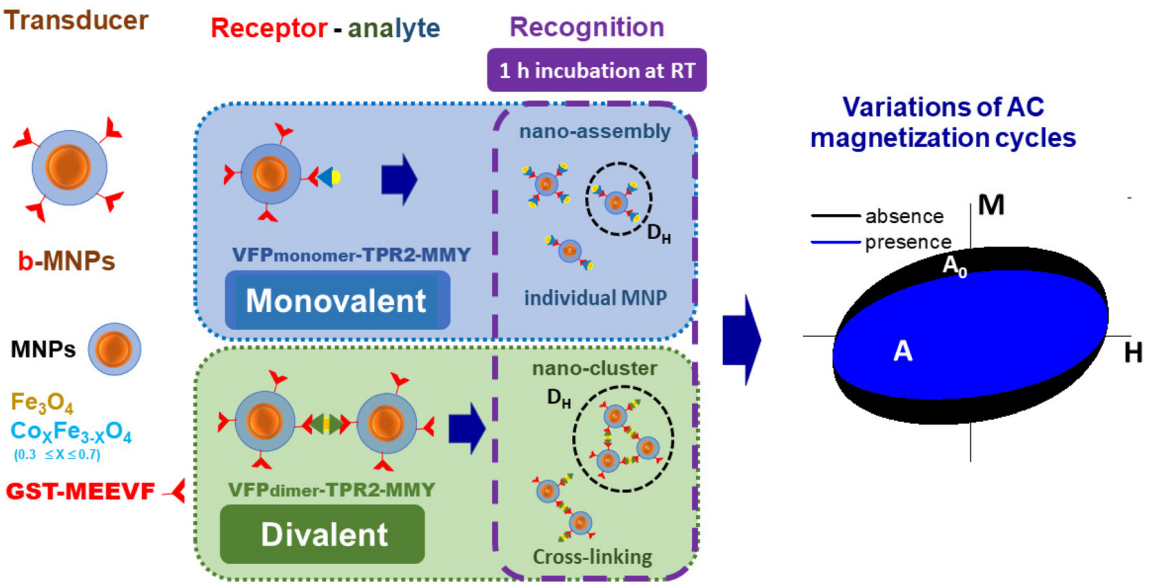

Fig. 1 Schematic representation of the detection method based on the variations of the AC magnetic hysteresis area in the absence (A_0) and presence (A) of VFP analyte variants. Individual (nano-assembly) or cross-linked (nano-cluster) assemblies are formed after biomolecular recognition between (GST-MEEVF) conjugated receptors and $VFP_{monomer}$ or VFP_{dimer} -TPR2-MMY variants. Incubation conditions: at given b-MNP and analyte concentrations dispersed in 0.1× PB for 1 hour at 25 °C in the absence of an external magnetic field.

Table 1 Summary of structural, and colloidal parameters of the studied MNPs when dispersed in DDW

MNP	Composition	Shape	TEM size (nm)	Coating	D_H intensity (nm)	D_H number (nm)	D_H volume (nm)	PDI	ξ potential (mV)
IONFs	Fe_3O_4	Nanoflower	30 ± 4	Dextran-PEG	65 ± 0.5	40 ± 2	53 ± 1.5	0.12	−5
IONPs	Fe_3O_4	Polyhedron	16 ± 4	DMSA	93 ± 0.4	21 ± 3.1	118 ± 0.4	0.19	−38
CoFeNFs	$Co_{0.3}Fe_{2.7}O_4$	Nanoflower	32 ± 5	Dextran	52 ± 0.6	41 ± 0.6	48 ± 0.6	0.08	−8
CoFeNCs	$Co_{0.7}Fe_{2.3}O_4$	Cubic	20 ± 3	PMAO	69 ± 26	37 ± 11	49 ± 0.2	0.12	−45

ACM under alternating magnetic fields whose field frequency ranges from 10 to 300 kHz and intensities up to 24 kA m^{-1}. Recent works[51] have shown the relevance of field conditions (*i.e.*, field frequency and intensity value) to define a measurement time (τ_M) in order to probe the dynamic magnetization loops. Indeed, we took advantage of selecting field conditions to optimize the observation of alterations of magnetic relaxation times following b-MNP nano-assembly or nano-cluster formation. These alterations are reflected in AC magnetization loops, and therefore the AC magnetic hysteresis area (A) is an adequate parameter to monitor the variations of dynamic magnetization loops in biomolecular recognition (see Fig. 1). Moreover, the normalization of the A value obtained in the presence of a given analyte concentration by the magnetic area value in the absence of analytes (A_0) offers an adequate parameter (A/A_0) to track the b-MNP transducing capacity under the experimental conditions studied in this work. In this manner, we studied the influence of different parameters on the transducing sensitivity of the proposed methodology, as shown in the next section.

Effect of MNP magnetic relaxation mechanisms on the b-MNP transducing capacity for monovalent analyte detection

To unveil the effect of the relaxation mechanisms on the b-MNP transducing capacity for detecting monovalent analytes, we employed bio-conjugated iron oxide (b-IONF) and cobalt ferrite (b-CoFeNF) nanoflowers. We also unveiled the prevalence of Néel or Brownian relaxation mechanisms in IONFs and CoFeNFs by looking at viscosity effects on AC magnetization cycles (see Fig. S1†). Afterwards, we performed DLS and ACM measurements to monitor the variations of D_H and A/A_0 in the presence of monovalent analytes. As shown in Fig. 2a, no significant variations of AC magnetization cycles were observed for b-IONF formulations on increasing the monovalent analyte concentration up to 4 μM. In contrast, Fig. 2b depicts remarkable variations of AC magnetization cycles (shape and values) for b-CoFeNF formulation in the same analyte concentration range. Then, a progressive reduction of the normalized magnetic area (A/A_0) is observed up to 30% at the highest analyte concentration (4 μM) for

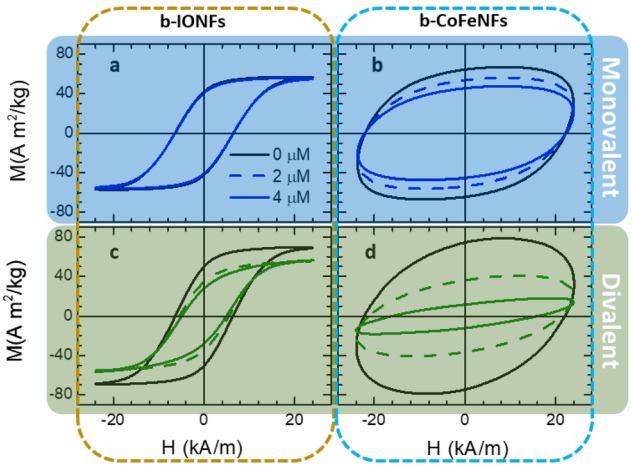

Fig. 2 AC hysteresis loops of b-IONFs (left) and b-CoFeNFs (right) after incubation with mono- and divalent analytes at different concentrations. AC magnetization measurements were performed under AC field conditions: (a and c) 100 kHz and 24 kA m^{-1}; (b and d) 30 kHz and 24 kA m^{-1}. Incubation conditions: b-MNPs (1 $g_{Fe\ or\ Fe+Co}$ per L) dispersed in 0.1× PB for 1 h at 25 °C.

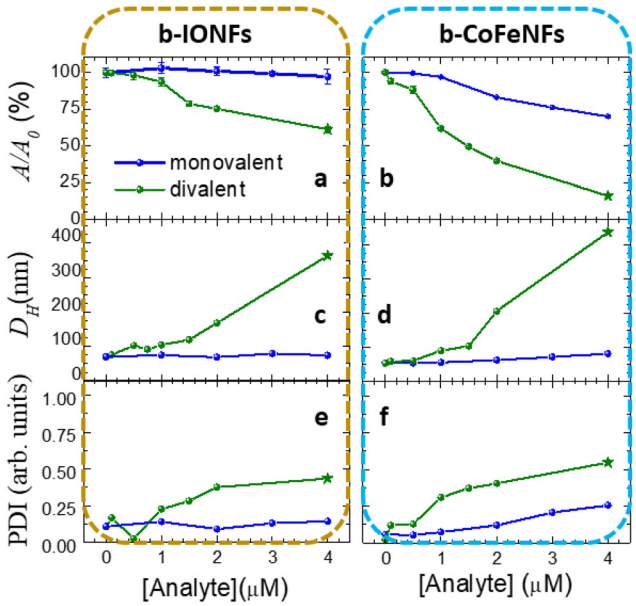

Fig. 3 Analyte concentration dependence of the normalised AC magnetic area (A/A_0) extracted from the AC hysteresis loops of (a) b-IONF suspensions at 100 kHz and 24 kA m^{-1} and (b) b-CoFeNF suspensions at 30 kHz and 24 kA m^{-1}. Analyte concentration dependence of D_H values obtained for: (c) b-IONF suspensions and (d) b-CoFeNF suspensions. Analyte concentration dependence of PDI values obtained for: (e) b-IONF suspensions and (f) b-CoFeNF suspensions. Incubation conditions: b-MNPs (1 $g_{Fe\ or\ Fe+Co}$ per L) dispersed in 0.1× PB for 1 h at 25 °C with increasing analyte mono- (blue colour) or di-valent (green colour) concentrations. Star symbols indicate the sedimentation of magnetic suspensions prior to magnetization measurements.

CoFeNFs. The origin of the distinct AC magnetization behaviour observed for IONFs and CoFeNFs after monovalent analyte recognition seems to be related to the distinct nature of their dominant magnetic relaxation process. On the one hand, the prevalence of the Brownian process for CoFeNFs allows the transduction of the monovalent recognition down to 50 nM, while b-IONFs (for which Néel relaxation prevails) do not transduce even at the highest analyte concentration. On the other hand, different MNP sizes, shapes and compositions just define the extent of the variation of AC hysteresis loops after biomolecular recognition (see Fig. S2† for IONPs and CoFeNCs). It is worth noting that the lowest analyte concentration (50 nM monomer VFP variant) detected by this magnetic method corresponds to the concentration values of clinical relevance.[15,16]

Besides, Fig. 3c and d show that intensity-weighted D_H values are maintained at around 65 ± 0.5 nm with a polydispersity index (PDI) smaller than 0.2 on increasing the monovalent analyte concentration for b-CoFeNFs and b-IONFs (see the blue dots in Fig. 3). Indeed, the nano-assembling phenomena mediated by monovalent biomolecular recognition keeps individually dispersed b-MNPs after incubation. Only CoFeNFs show some agglomeration at analyte concentrations higher than 2 μM due to some unspecific interactions mediated by magnetic interactions due to their MNP blocked magnetic state[52] (see Fig. S3†). Interestingly, the translational diffusion coefficient varies depending on the MNP surface (*i.e.* the bare, bio-conjugated receptor or analyte bound to the receptor). As shown in Table S1,† both IONF and CoFeNF nanoflowers show a 12% progressive decrease of the translational diffusion coefficient values upon conjugation and monovalent analyte recognition: from 10.3 ± 0.1/8.9 ± 0.5 × 10^6 nm^2 μs^{-1} for bare CoFeNFs/IONFs down to 9.1 ± 0.2/7.7 ± 0.4 × 10^6 nm^2 μs^{-1} for b-CoFeNFs/b-IONFs in the presence of 2 μM monovalent analyte, respectively. However, the variation of the diffusion coefficient is only reflected in the AC magnetization cycles measured for b-CoFeNFs due to the prevalence of Brownian relaxation mechanism. To confirm such an assumption, we performed numerical simulation of AC hysteresis loops by using the stochastic Landau–Lifshitz–Gilbert equation and the Brownian dynamics algorithm. AC hysteresis loops of IONFs and CoFeNFs were simulated when distinct magnetic relaxation processes prevail. As shown in Fig. 4, an outstanding agreement between experiments and numerical predictions is observed. Since b-MNPs remain individually dispersed in PB after biomolecular recognition, numerical simulations succeed to accurately describe the experimental observations just by considering the MNP dominant magnetic relaxation process and some experimental parameter values (see Tables S2 and S3†) including MNP diffusion coefficients. Our findings underline the relevance of the MNP magnetic relaxation mechanism for displaying the detection of monovalent analytes *via* AC magnetometry.

Effect of analyte multivalency on the transducing capacity of b-MNPs for analyte detection

To assess the effect of analyte multivalency on the transducing capacity of b-MNPs, we again employed b-IONF and b-CoFeNF

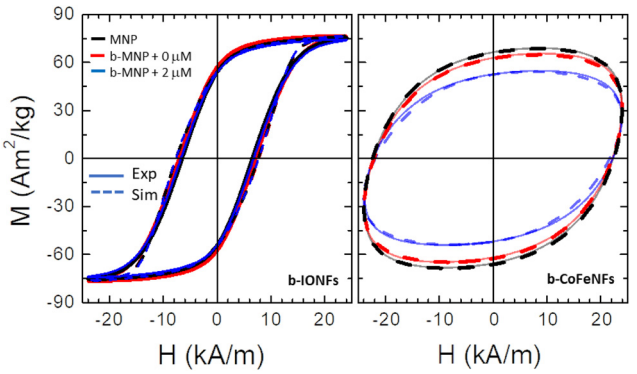

Fig. 4 Experimental (solid lines) and simulated (dashed lines) AC hysteresis loops for: (left) IONFs (black line) and b-IONFs in the absence (red line) and presence (blue line) of monovalent analytes at 100 kHz and 24 kA m^{-1}; (right) CoFeNFs (red line) and b-CoFeNFs in the absence (black line) and presence (blue line) of monovalent analytes at 40 kHz and 24 kA m^{-1}. Incubation conditions: b-MNPs (1 $g_{Fe\ or\ Fe+Co}$ per L) and 2 μM monovalent analytes dispersed in 0.1× PB for 1 h at 25 °C.

formulations incubated under the standard conditions (1 $g_{Fe\ or\ Fe+Co}$ per L of b-MNPs dispersed in 0.1× PB for 1 hour at 25 °C) with the divalent analyte variant in a concentration range from 0 to 4 μM. The biomolecular recognition of divalent analytes is expected to cross-link multiple b-MNPs and analytes, resulting in nano-clusters with larger D_H than those of individual b-MNPs. In contrast to the monovalent case, variations of AC hysteresis loops are now observed for all b-MNPs after biomolecular recognition (see Fig. 2c and d). Indeed, Fig. 3 shows the increase of the intensity-weighted D_H values for b-CoFeNFs and b-IONFs on increasing the divalent analyte concentration. The D_H increase is highly correlated to the PDI, which reflects the strong variability of nano-cluster formation (see Table S4†), as recently predicted.[38] This clustering is commonly observed for all b-MNPs regardless of their size, morphology, or coating (see Fig. S4† for b-IONP and b-FeCoNCs). However, the extent of changes in AC magnetization loops strongly depends on the b-MNP morphology and composition being more pronounced for b-CoFeNFs. Thus, divalent analyte contents down to 50 nM (*i.e.*, 2 mg of protein per liter) are detectable under standard b-MNP formulation and incubation conditions (*i.e.* 20 receptors per b-MNP and 1 $g_{Fe\ or\ Fe+Co}$ per L). At high analyte contents, A/A_0 values reduce up to 25 (40)% for b-IONFs and up to 60 (80)% for b-CoFeNFs (see the green dots in Fig. 3a and b) in the presence of 2 (4) μM divalent analyte. Such strong differences in the AC magnetic hysteresis area are understood in terms of D_H values and intra-cluster magnetic dipolar interactions.[39] Both parameters strongly influence Brownian and Néel magnetic relaxation processes, respectively. The linear correlation[53] between the Brownian relaxation time and the hydrodynamic volume renders CoFeNFs more sensitive to clustering effects than IONFs. On the other hand, the changes of the Néel relaxation time are due to the alteration of effective anisotropy *via* magnetic dipolar interactions, which tightly depend on the number of MNPs and their spatial distribution into the nano-clusters.[49,50,54] Therefore, our observation underlines the relevance of nano-cluster formation to detect divalent analytes by AC magnetometry regardless of the magnetic relaxation process.

Effect of b-IONF concentration on the transducing capacity for analyte detection

To assess the effect of the MNP concentration on the transducing capacity of b-MNPs, we studied the colloidal and dynamic magnetization of b-IONFs incubated under the standard conditions on increasing the b-IONF concentration values above the AC magnetometer sensitivity (≈0.3×10^{-3} Am^2) from 0.5 up to 2 g_{Fe} per L at a constant divalent analyte concentration of 0.75 μM. Qualitatively, it is intuitive that the MNP concentration would tightly influence cluster formation mediated by cross-linking between multiple b-IONFs and divalent analytes. Crosslinking phenomena tightly depend on the number of receptors per b-MNP, molecular recognition affinity, and analyte and b-MNP concentrations. Recent computational studies[38] correlate these key parameters with nano-cluster formation in terms of their size and fractal MNP spatial distribution at the limit of high receptor–analyte affinity. Fig. 5 depicts the D_H, PDI and normalized AC magnetic hysteresis area (A/A_0) extracted from the AC hysteresis loops measured at

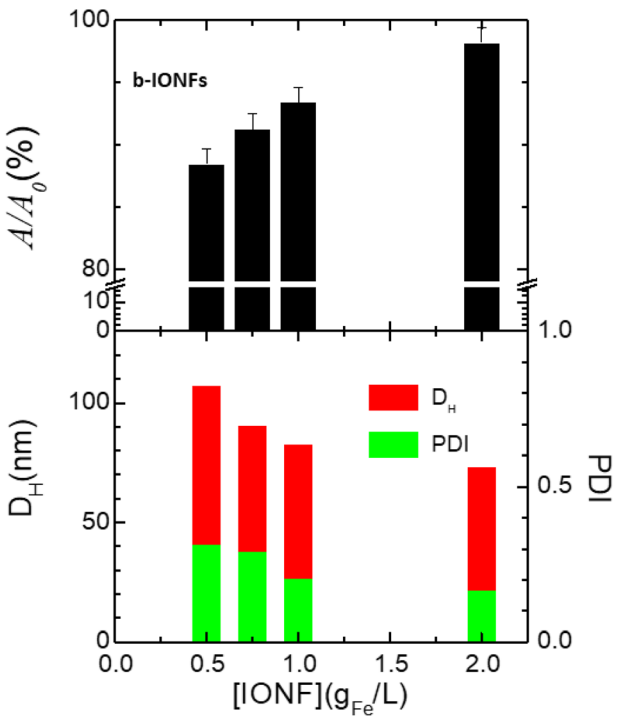

Fig. 5 b-IONF concentration dependence of the normalised AC magnetic area (A/A_0) and D_H and PDI values. Incubation conditions: 0.75 μM divalent analyte concentration and increasing IONF concentrations from 0.5 up to 2 g_{Fe} per L dispersed in 0.1× PB for 1 h at 25 °C. AC hysteresis loops were measured at 100 kHz and 24 kA m^{-1}.

100 kHz and 24 kA m^{-1} on increasing the iron concentration. At a first glance, we observed a strong reduction of D_H values from 110 down to 65 nm on increasing the MNP concentration 4-fold, while the PDI significantly decreases from 0.3 down to 0.14. In fact, AFM experiments reveal large variability in the spatial distribution of b-IONF into nano-clusters (see Fig. S5†). Low MNP concentrations result in high D_H and PDI values at the studied analyte concentration (0.75 μM). Such behavior can be understood in terms of the increase of receptor availability to specifically interact with divalent analytes when increasing the b-IONF content. In other words, the probability of sharing divalent analytes among b-IONFs decreases on increasing the number of bio-conjugated nanoparticles. This is because the number of available receptors increases, and consequently, D_H and PDI diminish. As shown in Fig. S5,† the absence of an external magnetic field during incubation leads to a random spatial distribution of IONFs into nano-clusters, which is exclusively mediated by biomolecular recognition, *i.e.* the receptor–analyte affinity, and the number of receptors, MNPs, and analytes present in 0.1× PB. As mentioned above, the evolution of D_H *versus* the MNP concentration determines the dynamic magnetization response, and consequently, the transducing capacity of b-IONFs. In this regard, larger clusters favor magnetic dipolar interactions,[39,48,54,55] which strongly influence Néel relaxation. Fig. 5 depicts the MNP concentration dependence on the normalized A/A_0 hysteresis area, resulting in a progressive increase from 85% up to 97% with decreasing D_H. Our observation underlines the relevance of MNP concentration to modulate the nano-cluster formation, influencing D_H and PDI. Interestingly, the transducing capacity of b-MNPs benefits from low b-MNP concentrations (<1 g_{Fe} per L) to detect divalent analytes.

Effect of the number of receptors per MNP on the b-MNP transducing capacity for analyte detection

To assess the effect of the number of receptors per b-MNP on the transducing capacity of b-MNPs, we probed the influence of the number of receptors (*i.e.*, recognition ligands) per b-MNP on their transducing capacity by studying IONFs bioconjugated with a distinct number of receptors bound onto the nanoparticle surface, ranging from 2 to 12 receptors per MNP. Next, b-IONFs were incubated under the standard conditions with 1 μM divalent analyte. Fig. 6 shows the MNP–receptor ratio dependence of colloidal and AC magnetic properties (*i.e.* D_H, PDI, and normalized AC magnetic hysteresis area at 100 kHz and 24 kA m^{-1}). The results reflect the significant variation of D_H and PDI on increasing the number of receptors per MNP. On the one hand, larger D_H and PDI values are observed for the lowest MNP–receptor ratio (1 : 2), reaching values D_H = 214 nm and PDI = 0.55. On increasing the ratios, D_H and PDI values progressively decrease down to 90 nm and 0.15, respectively. On the other hand, A/A_0 values progressively increase from 85% up to 100% when the receptor–MNP ratios increase. Similarly to the study of b-MNP and analyte concentration effects, the AC magnetic hysteresis area behavior is tightly related to the evolution of D_H values when MNP-receptor ratios vary. Interestingly, large ratios result in less efficient magnetic transduction. The reason is that the need for sharing divalent analytes between b-IONFs diminishes on increasing the number of receptors per particle. Consequently, D_H and PDI values shrink. Our experimental observations underline the role played by the number of receptors per MNP in cluster formation. Indeed, the MNP–receptor ratio effectively controls MNP cluster formation, and consequently, strongly influences the AC magnetization cycles. Interestingly, the transducing capacity of b-MNPs benefits from low number of receptors per nanoparticle in the studied analyte concentration range.

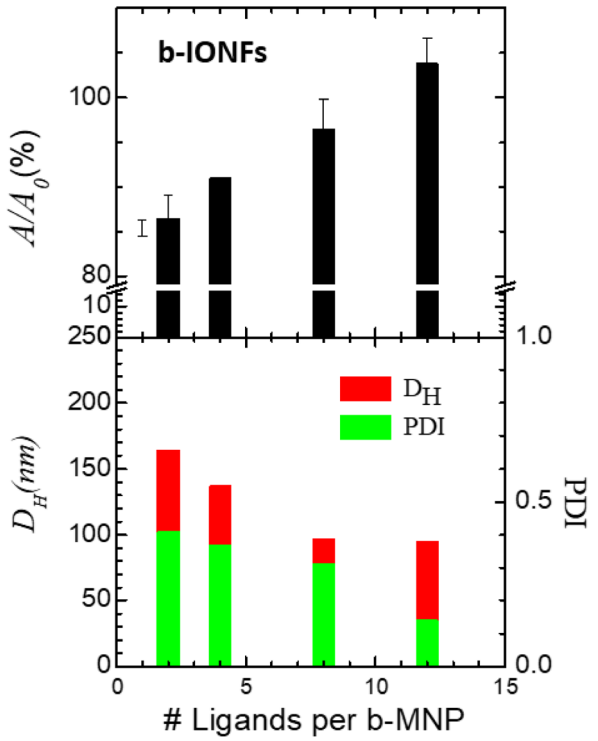

Fig. 6 Normalised hysteresis area (A/A_0) and D_H and PDI values of b-IONFs conjugated with a distinct number of receptors per MNP. Incubation conditions: different b-IONF receptor formulations at 1 g_{Fe} per L and 1 μM divalent analytes dispersed in 0.1× PB for 1 hour at 25 °C. AC hysteresis loops were measured at 100 kHz and 24 kA m^{-1}.

Effect of field conditions on the transducing capacity of b-MNPs for analyte detection

To assess the role of the field conditions in analyte detection, we incubated the prepared b-IONFs and b-CoFeNFs with 2 μM of mono- or divalent analytes under the standard conditions described in previous sections. AC magnetization measurements were performed under alternating magnetic fields ranging from 10 up to 100 kHz and field intensities up to 24 kA m^{-1}. As shown in Fig. S6,† the A and A_0 values tightly depend on field conditions, as well as the presence of analyte and MNP compositions. At a first glance, A values observed for CoFeNFs are twice larger than those for b-IONFs. In addition,

the frequency dependence of the CoFeNF AC magnetic area shows a trend of decrease/raise-saturation-decrease of their hysteresis area values at 4/24 kA m^{-1} intensity values, respectively. In contrast, the AC magnetic area frequency behaviour remarkably differs for IONFs with the field intensity. At 4 kA m^{-1}, a progressive decrease of the AC magnetic area is observed on increasing the field frequency value. At 24 kA m^{-1}, the AC magnetic area progressively increases (in Fig. S6†). Such a different behaviour for IONFs and CoFeNFs is understood by the appearance or not of minor cycles on increasing f (see Fig. S7†). Except for b-IONFs incubated with monovalent analytes, biomolecular recognition phenomena in general reduce the AC magnetic area values with respect to the case in the absence of analytes. To better quantify the variation of sensitivity under different field conditions, we monitored A/A_0 in Fig. 7, where the values range from 100% down to 65% depending on MNP composition, analyte valency and field conditions. For b-CoFeNFs, we observed a larger decrease of A/A_0 values for the divalent analytes than for the monovalent ones, which maintain values of around 70% almost independent of field conditions. For b-IONFs, A/A_0 values are maintained around zero for the monovalent case under all field conditions. However, for the divalent case, IONFs showed a progressive decrease of A/A_0 values on increasing the field frequency from 100 down to 90% at 24 kA m^{-1}, while A/A_0 values are maintained around 80% at 4 kA m^{-1}. The influence of field conditions on analyte detection sensitivity can be understood in terms on how AC hysteresis loops is tailored by the external AC magnetic field. Recent magnetic studies[45] show the induced field transition between magnetically unblocked and blocked states. The field frequency (f) defines the measurement time ($\tau_m = 1/2\pi f$) according to the magnetic field sweeping rate during magnetization measurements. Thermal fluctuations across the magnetic anisotropy barrier are behind the relaxation mechanism that determines the lag between the external field and magnetic moment directions. Such a time lag tailors the opening of AC magnetization cycles.[51] Moreover, field intensity (H_0) defines both the number of the MNP magnetic moments aligned with respect to the external field direction and the magnetic regime (linear or non-linear) in which magnetization dynamics occur. In this manner, the field frequency and intensity probe MNP magnetic relaxation, defining the shape and values of AC magnetization cycles, as shown in Fig. S7.† Interestingly, our experimental evidence shows how field conditions remarkably influence the transduction capacity of the studied MNPs. Indeed, low field intensities benefit the observation of A/A_0 variations for more sensitive detection of divalent analytes (*i.e.* nano-clustering) in CoFeNFs (*i.e.* Brownian relaxation).

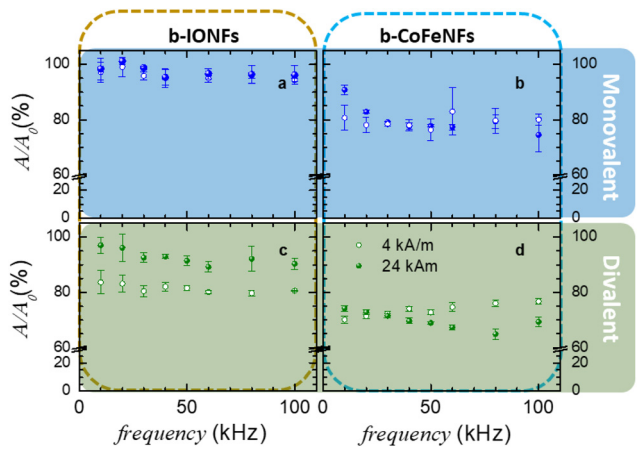

Fig. 7 Frequency dependence of A/A_0 at two field intensities (4 and 24 kA m^{-1}) for: (a) b-IONFs and monovalent analytes (blue colour); (b) b-CoFeNFs and monovalent analytes (blue colour); (c) b-IONFs and divalent analytes (green colour); and (d) b-CoFeNFs and divalent analytes (green colour). Incubation conditions: b-MNPs (1 g_{Fe+Co} per L) dispersed in 0.1× PB for 1 h at 25 °C at 2 μM of monovalent and divalent analytes. Data extracted from Fig. S6.†

Conclusions

We report on the proof of concept and parametrization of a novel and highly sensitive methodology for quick and direct detection of proteins dispersed in liquids. This methodology is based on the variation of the AC magnetic hysteresis area from b-MNPs upon specific interactions with two analyte variants. We have assessed the effect of several parameters on the MNP transducing capacity. First, our observations underline the relevance of the dominant MNP magnetic relaxation nature for transducing the biomolecule interactions with b-MNPs under alternating magnetic fields. The Brownian process benefits the transduction of specific interactions between b-MNPs and monovalent/divalent analytes with respect to the Néel mechanism. Second, the analyte valence defines assembling phenomenology leading to nano-assemblies (*i.e.* surface modifications) or nano-clusters (*i.e.* agglomeration of MNPs and cross-linked analytes), enabling analyte detection down to 0.05 and 4 μM. Numerical simulations support our hypothesis regarding surface modification effects on cobalt ferrite nanoparticles for monovalent detection, showing an outstanding agreement with the experimental results. Third, the number of b-MNPs and receptors per MNP influences nano-cluster formation in a similar manner to the analyte content. Interestingly, the transducing capacity of b-MNPs also benefits from a low MNP concentration and a low number of receptors per MNP for analyte detection. Finally, the field conditions benefit the observation of changes of AC magnetization cycles after biomolecular recognition. The systematic description of the parameters tuning the sensitivity of the proposed methodology allows a precise sensing customization by tailoring the b-MNP design and AC magnetometry settings. In this manner, clinical biomarkers can be adequately detected by separately testing the relevance of each studied parameter in the sensitivity modulation. This approach will provide optimal detection settings for employing the proposed biosensing methodology as an alternative *in vitro* diagnosis test.

Experimental section/methods

Magnetic nanoparticles

Table 1 lists some structural and colloidal features of the four MNPs employed in this study: (1) commercial magnetite nanoflowers (IONFs) (Synomag®-D, product code: 104-56-701, Micromod Partikeltechnologie GmbH, Germany) coated with carboxylic poly(ethylene glycol) (PEG) with a nanocrystal size of 30 ± 4 nm; (2) commercial maghemite nanoparticles (IONPs), supplied by Liquid Research Ltd, United Kingdom (product: HYPERMAG C), coated with carboxylic dimercaptosuccinic acid (DMSA) with a nanocrystal size of 16 ± 4 nm; (3) commercial $Co_{0.3}Fe_{2.7}O_4$ nanoflowers (CoFeNFs) (product code: 124-02-501; Micromod Partikeltechnologie GmbH, Germany) coated with carboxylic dextran with a nanocrystal size of 32 ± 5 nm; and (4) $Co_{0.7}Fe_{2.3}O_4$ nanocubes (CoFeNCs) coated with carboxylic with poly(maleic anhydride-alt-1-octadecene) (PMAO) with a cube edge size of 20 ± 3 nm. The CoFeNCs were synthesized by the thermal decomposition method following a procedure described elsewhere.[56]

Nanocrystal size

The MNP size and shape were evaluated by TEM (see Fig. S8†). A JEOL 2100 microscope operating at 200 kV (point resolution 0.18 nm) at the Centro Biología Molecular Severo Ochoa UAM-CSIC was employed. TEM images were examined through manual analysis of more than 150 particles randomly selected in different grid locations using Image-J software to obtain the mean size and size distribution, as listed in Table 1.

Quantification of iron content in the magnetic colloids

The Fe and Co concentrations in the studied MNP magnetic suspensions were determined by inductively coupled plasma optical emission spectrometry using an ICP-OES (PerkinElmer Optima 2100 DV) at Servicio de Análisis Químico, ICMM-CSIC (Madrid, Spain).

Receptors and analytes

The receptor (or the recognition ligand) was the glutathione *S*-transferase (GST) protein fused at the C-terminal end to an engineered peptide of 24 amino acids with a final MEEVF sequence (GST-MEEVF) for specific recognition of the MMY-TPR2 domain.[46] This domain has been fused to a monomeric or dimeric variant of the VFP, resulting in mono-($VFP_{monomer}$-TPR2-MMY)[47] and divalent (VFP_{dimer}-TPR2-MMY) variants with one or two recognition sites, respectively. This strategy offers the VFP with single or multivalencies interacting with the same GST-MEEVF receptor.

MNP bio-conjugation

For the bio-conjugation of the employed MNP formulations, we took advantage of carboxylic groups present in all coatings listed in Table 1. To activate the present carboxylic groups in dextran, PEG and DMSA were coated with CoFeNFs, IONPs, and IONFs, respectively, 1 mL of MNPs at 2.5 g L^{-1} of magnetic element mass (Fe or Fe + Co) were incubated 4 hours at 37 °C with 150 mmol EDC per g of Fe/Fe + Co and 150 mmol EDC per g of NHS Fe/Fe + Co. Then, the MNP suspension was washed using centrifugal filters (amicon ultra) with a molecular weight cut off (MWCO) of 100 kDa. Next, b-MNPs were redispersed in 10 mM sodium phosphate buffer at pH 7.4 to a final volume of 1 mL and the filter cleaning was repeated three times. These MNPs with pre-activated carboxyl groups were incubated at 2.5 $g_{Fe/Fe+Co}$ per L with 100 µl of 167 µM GST-MEEVF fusion protein in PB overnight at 37 °C. Finally, b-MNPs were purified by gel filtration through a sepharose 6 CLB column using PB. Diffusion measurements of b-MNPs and MNPs were performed to assess the presence of bio-conjugated GST-MEEVF on the MNP surface, resulting in translational diffusion changes. To activate the present carboxylic groups in CoFeNCs coated with PMAO,[57] 1 mL of CoFeNCs at 2.5 g_{Fe+Co} per L was incubated for 4 hours at 37 °C with 150 mmol EDC per g of Fe + Co, 75 mmol NHS per g of Fe + Co and 10 µL of NaOH 1M. After that, the same GST-MEEVF bio-conjugation procedure was employed for IONFs and IONPs.

Preparation of b-MNPs with different numbers of receptors

First, a nanoparticle tracking analysis (NTA) was performed (Nanosight NS300, Malvern, UK) to determine the hydrodynamic size, translational diffusion coefficient, and the number of particles per mL (1.9×10^{12} IONF per mL) by diluting a IONF solution at 1 g_{Fe} per L in a 1 : 5000 ratio in double distilled water (DDW). Second, in order to set the bio-conjugation protocol to anchor a single receptor per MNP, we took 500 µL of each MNP suspension at 2.5 g_{Fe} per L and pre-activated according to the previous protocol using 150 µmol EDC per g_{Fe} and 75 µmol NHS per g_{Fe} (4 hours at 37 °C). Later, it was washed using a centrifugal filter (amicon ultra) and redispersed in PB to a final volume of 1 mL. Carboxyl pre-activated MNPs were incubated overnight at 37 °C with 5 µL of 3 µM GST-MEEVF to establish a 1 GST-MEEVF: 1 MNP ratio. Afterwards, b-MNPs decorated with the GST-MEEVF fusion protein was purified by filtration using a sepharose 6 CLB column and concentrated to a final volume of 1 mL and a MNP concentration of 1 g_{Fe} per L. Taking advantage of the analyte fluorescence, single molecule fluorescence spectroscopy was employed to quantify the number of receptors (*i.e.*, ligands) present on the b-MNP surface after incubation with monovalent analytes. We intentionally prepared a b-MNP formulation with a MNP : receptor ratio of 1 : 1 and characterized by single fluorescence spectroscopy (SFS), as described in the next section. This allows us to set the bio-conjugation procedures of MNPs at distinct MNP : receptor ratios of 1 : 2, 1 : 4, 1 : 8, and 1 : 12. For this, we added different volumes of GST-MEEVF at 3 µM (10 µL, 20 µL, 40 µL and 70 µL, respectively) to the pre-activated MNPs.

Quantification of the number of recognition receptors

Single fluorescence spectroscopy was employed in order to accurately determine the average number of bio-conjugated recognition ligands per b-MNP and their particle distribution.

In brief, fluorescent analytes attached to the immobilized MNPs were photobleached one at a time while monitoring the time evolution of analyte fluorescence intensity from the analytes bound to receptors per MNP (Fig. S9†). The spatially-localized intensity changes related to single-fluorophore photobleaching show the number of fluorophores[58] at the particular location of b-MNPs on the coverslip. To prepare the sample for SFS, glass substrate coverslips (25 × 75 mm type #1.5 glass) were first cleaned with piranha solution and coated with a mixture of PEG5000 (Iris Biotech GmbH, Germany) and PEG10000-biotin (Iris Biotech GmbH, Germany) mixture (1 : 10 000) before adding streptavidin (Thermo Fisher Scientific) to fix the biotinylated b-MNPs. Then, the biotinylated b-MNPs were released to immobilize MNPs onto the coverslip. Single MNP photobleaching experiments were carried out using a custom-made total internal reflection fluorescence (TIRF) microscope.[59] An oil immersion objective UAPON 100× OTIRF (Olympus) was set on an IX73 Olympus microscope body. A 488 nm continuous wavelength laser (Sapphire, Coherent,USA) was used to excite the analyte fluorescence at 520 nm. The excitation laser power was 10 mW (epifluorescence configuration) at the objective. The filter cube used was ZET405/488/561m-TRF (Chroma). An Andor iXon 897 EMCCD camera was used for aquiring 512 × 128 pixel-images with the electron multiplier set to 300 and 17 MHz readout rate. A continuous sequence of 1500 20 ms frames was acquired for the analysis of photobleaching steps. Data analysis was performed in two steps. First, fluorescent complexes bound to the MNPs were spatially localized using free software RapidStorm.[60] An fluorescence intensity trace was obtained for every MNP in the 1500frame sequence. Second, the intensity traces for every MNP were subsequently analyzed with in-house developed software (MatLab). The employed software inputs are shown in Table S5.† Only fluorescent complexes that showed a maximal to minimal intensity difference equal or larger than the fluorescence intensity of a single $VFP_{monomer}$-TPR2-MMY analyte (previously calibrated) were considered. Accordingly, intensity changes were only counted as a bleaching step if the intensity change was equal or larger than single $VFP_{monomer}$-TPR2-MMY. To prevent misidentification due to blinking or noise events, it was required that intensity changes lasted for at least five consecutive frames (100 ms). These conditions were adapted to the nanoparticle fluorescent complexes from the literature.[61,62] After filtering the fluorescent complexes and the photobleaching steps described above, the photobleaching steps were counted on each fluorescent b-MNP to perform statistical analysis to determine the number of receptors per MNP (see Fig. S10†). For all experiments a minimum of 5000 particles were analyzed.

Analyte and b-MNP incubation conditions

50 μL of the MNP formulations at the given MNP content ranging from 0.5 up to 2 $g_{Fe/Fe+Co}$ per L were incubated in 0.1× PB for 1 hour at 25 °C with different analyte variants at distinct analyte concentrations from 0 (control) up to 4 μM. All incubations were performed in the absence of external magnetic fields.

Hydrodynamic size measurements

DLS measurements were performed to determine the intensity, number and volume-weighted D_H of the b-MNPs under different experimental conditions. For that purpose, we employed a Zetasizer Nano ZS90 (Malvern Instruments, United Kingdom) equipped with a 4 mW He–Ne laser operating at 633 nm as an energy source with an angle of 173° between the incident beam and the avalanche photodiode detector. DDW and PB were used as dispersion media for measuring the colloidal properties of MNPs before bio-conjugation. Otherwise, the colloidal properties of b-MNPs at different MNP and analyte concentrations were studied in 0.1× PB. b-MNPs were diluted to a final MNP concentration of 0.05 $g_{Fe/Fe+Co}$ per L in 1 mL volume deposited into a commercial cuvette prior automatic scan measurements (three scans per measurement).

Diffusion coefficient measurements

Table S1† lists the translational diffusion coefficients of IONFs and CoFeNFs in 0.1× PB obtained by NTA (Nanosight NS300, Malvern Instruments, United Kingdom). Bare and bio-conjugated MNP suspensions at an initial concentration of 1 $g_{Fe/Fe+Co}$ per L were diluted to 1 : 5000 in 0.1× PB and injected into the instrument chamber using a 1 mL syringe. Camera settings were adjusted to focus the objective and track the individual Brownian motion of 20–80 MNPs in the camera cell (see Fig. S11†). Video data were recorded for 30 seconds and repeated 5 times per sample.

Magnetic characterization

Magnetization cycles under quasi-static conditions of MNPs dispersed in DDW were performed at different temperatures (4 and 300 K) using a Quantum Design SQUID magnetometer model MPMS-XL at Técnicas Físicas, Universidad Complutense de Madrid (Madrid, Spain). The measured samples were 100 μL of MNP dispersion volumes at a concentration of 1$g_{Fe/Fe+Co}$ per L. The magnetization values were normalized to the magnetic element mass (Fe or Fe + Co) of each measured suspension (see Fig. S12 in the ESI†). AC magnetometry measurements of the magnetic colloids with a magnetic element mass ranging from 20 up to 80 μg were performed using commercial inductive magnetometers (SENS and ADVANCE AC Hyster™ Series, Nanotech Solutions, Spain). AC Hyster Series magnetometers measure magnetization cycles of MNPs dispersed in liquid media at room temperature under alternating magnetic fields whose frequency ranges from 10 up to 300 kHz and intensities up to 24 kA m^{-1}. Each AC magnetization measurement consists of three repetitions to obtain an average of the magnetization cycles and the related magnetic parameters (H_C, M_R, and AC magnetic hysteresis area). Such dynamic magnetization measurements take less than 60 seconds. Magnetization units were normalized by the magnetic element mass (*i.e.*, iron or iron plus cobalt magnetic elements) and expressed in $Am^2\ kg^{-1}$.

Computational simulations

Numerical simulations of MNPs' AC magnetization cycles were performed to understand the AC magnetic hysteresis area behaviour observed for the CoFeNF and IONF nano-assemblies by using multiphysics UAMMD software.[63,64] The latest is an open source framework running in graphical processor units equipped with an immersed boundary[65] and Brownian-based[66] colloidal hydrodynamics, recently generalised to include magnetic interactions between MNPs. Notably, the magnetic-UAMMD uses the single domain approach to solve the internal dynamics of magnetization involving Néel relaxation and their coupling with MNP Brownian motion. The internal dynamics of MNP magnetization $\vec{m}(t)$ is solved by integrating the Landau–Lifshitz–Gilbert equation, following the scheme used in Vinamax code:[67]

$$\frac{d\vec{m}}{dt} = \frac{-\gamma_0}{1+\alpha^2}(\vec{m}\times\vec{B}_{eff} + \alpha\vec{m}\times\vec{m}\times\vec{B}_{eff})$$

where $\gamma_0 = 1.7595 \times 10^{11}$ rad Ts^{-1} denotes the gyromagnetic ratio, α is the Gilbert damping constant, and $\vec{m}(t)$ is a unitary vector parallel to the direction of the MNP magnetic moment; $\vec{B}_{eff} = \vec{B}_{an} + \vec{B}_{th} + \mu_0\vec{H}_{AC}$ is the effective magnetic field acting on each MNP composed of the anisotropy field ($\vec{B}_{anis}$), the thermal field ($\vec{B}_{therm}$), and the external magnetic field ($\vec{H}_{AC}$). Note that the dilute MNP concentration employed in the experiments allows for neglecting magnetic interacting phenomena between MNPs. The anisotropy field was calculated as:

$$\vec{B}_{anis} = \frac{2K}{M_{sat}}\cdot(\vec{m}\cdot\hat{u})\cdot\hat{u}$$

where K is the MNP anisotropy constant, M_{sat} is the saturation magnetization value of the MNP ensemble, and $\hat{u}$ is the unit vector denoting the easy axis direction of MNPs. The thermal field described the effect of thermal fluctuations arising from the MNP magnetic mono-domain and satisfies the fluctuation–dissipation relationship derived by Brown:[68]

$$\vec{B}_{therm} = \sqrt{\frac{2k_BT\alpha}{\gamma_0 M_{sat} V_c dt}}\cdot\vec{W}$$

where k_B denotes the Boltzmann constant, T is the temperature of the system, V_c is the volume of the magnetic core of the particles, dt is the time step, and $\vec{W}$ represents a random vector whose components follow a normal distribution with zero mean and uncorrelated in time and space $\langle W_i(t)\ W_j(0)\rangle = \delta(t)\ \delta_{ij}$. The external magnetic field ($\vec{H}_{AC}$) defined by a time dependent sinusoidal wave with field amplitude (*i.e.* intensity) H_0 and frequency f:

$$\vec{H}_{AC} = \vec{H}_0\cdot\sin(2\pi f\cdot t)$$

On the other hand, the Brownian motion of each MNP is simulated by solving the overdamped Languevin equation. Given that we are neglecting all interactions between particles, we do not need to solve the translational movement of the particles, and we only solve their angular motion. In every step we rotate each particle using a rotation vector $d\vec{\phi}$ computed as follows:

$$d\vec{\phi} = -M_r\cdot\ \overrightarrow{\tau_{AC}}\cdot dt + \sqrt{2k_BTM_r}\cdot\overrightarrow{dW}$$

where $\overrightarrow{dW}$ is a vector of independent Wiener increments (three random components with zero mean and unit variance, *i.e.* $\langle dW_i^2\rangle = dt$). We used $M_r = \frac{1}{\pi\eta {D_H}^3}$ for the rotational mobility of a spherical colloid, while $\overrightarrow{\tau_{AC}}$ is the torque exerted by the field on the particles:

$$\overrightarrow{\tau_{AC}} = \mu_0\cdot\vec{M}\times\overrightarrow{H_{AC}}$$

where $\vec{M} = M_{sat}\cdot V_C\cdot\vec{m}$ is the MNP magnetic moment. Values of M_{sat} and K were obtained from quasi-static magnetization measurements at 4 and 300 K (see Table S2†). V_c was obtained from the MNP TEM images. Simulations considered the MNP size Gaussian distribution, mean size and standard deviation observed from the TEM images (see Table S3†). Depending on the predominant relaxation mechanism of the particles (*i.e.* Brown or Néel), the procedure employed to simulate the cycles was slightly different. When the predominant mechanism is Néel, AC magnetization cycles are not sensitive to changes in the hydrodynamic size. Hence, it was enough to perform the simulations using the same hydrodynamic size for all the particles. The value of the hydrodynamic size was obtained from the experimental measurements of the translational diffusion coefficient of the particles (Table S1†). In contrast, when the predominant relaxation mechanism is Brown, AC magnetization cycles are extremely sensitive to change the distribution of hydrodynamics sizes. For that reason, it was necessary to consider not only the mean hydrodynamic size of the particles, but also their distribution. In this simulations we have considered a log–normal distribution of hydrodynamic sizes:[69–71]

$$p(D_h) = \frac{1}{D_h\sigma\sqrt{2\pi}}\exp\left(-\frac{(\ln(D_h)-\mu)^2}{2\sigma^2}\right)$$

where μ and σ are the mean hydrodynamic size (D_h) and the standard deviation of the distribution (STD) through:

$$\mu = \ln\left(\frac{{D_h}^2}{\sqrt{{D_h}^2+\mathrm{STD}^2}}\right)$$

$$\sigma^2 = \ln\left(1+\frac{\mathrm{STD}^2}{{D_h}^2}\right)$$

The values of D_h and STD were determined by performing unbiased random samplings in which both magnitudes (employed as input parameters for the simulations) were varied until the experimental magnetization cycles were accurately fitted. In order to speed up these samplings, we benefited from the large anisotropy energy in comparison with thermal energy, *i.e* $KV \gg k_BT$. In this way, the rigid dipole approximation[72–74] (*i.e.* $\vec{M}$ aligned to the MNP magnetization easy axis) is assumed. Hence, we avoided the costly calculation of the internal dynamics of magnetization, which otherwise requires quite small time steps, in comparison with those

employed for solving MNP Brownian motion. Once the optimal MNP size distribution was found, we removed the adiabatic approximation for the magnetization vector and reproduced the experimental cycles solving the Landau–Lifshitz–Gilbert equation to verify the validity of this approach.

Author contributions

F. J. T. and A. L. C. designed the research. N. S. and T. P. synthesized and characterized the CoFeNCs. E. S. D., A. A., D. C., and E. J. A. I. performed the bio-conjugation, DLS, NTA and AC magnetization experiments. P. P. A. and R. D. B. performed the simulations. C. C. V. and J. R. I. performed the single-molecule fluorescence experiments. E. S. D., A. A., D. C., A. L. C., and F. J. T. analyzed and discussed the results. E. S. D. and F. J. T. wrote the first draft and the remaining authors contributed to tail the submitted and revised manuscript.

Conflicts of interest

There are no conflicts to declare.

Acknowledgements

This work was partially funded by the Spanish State Research Agency (PCI2019-103600, CEX2020-001039-S, MDM-2017-0720, PID2019-111649RB-I00, PID2020-117080RB-C51, PID2020-117080RB-C53, PID2019-111649RB-I00, PDC2021-120957-I00, PDC2022-133345-I00, and Hipernano, RED2018-102626-T, PTA2018-015076) and Comunidad de Madrid (PEJ-2017-AI/BMD-7517, PEJ-2020-AI/IND-19394, NANOMAGCOST S2018/NMT-4321). COST Actions CA17115 (MyWave) and CA17140 (Nano2Clinic) were also acknowledged. This work was partially supported by the European Union's Horizon 2020 research and innovation programme under the Marie Sklodowska-Curie HeatnMof grant (GA No. 860942).

References

1 F. Vahedifard and K. Chakravarthy, *Emergent Mater.*, 2021, **4**, 75–99.
2 S. B. Nimse, M. D. Sonawane, K.-S. Song and T. Kim, *Analyst*, 2016, **141**, 740–755.
3 C. L. Sawyers, *Nature*, 2008, **452**, 548–552.
4 N. Shaabani, S. R. Meira, M. Marcet-Palacios and M. Kulka, *ACS Pharmacol. Transl. Sci.*, 2023, **6**, 387–398.
5 X. Wang, R. Xu, X. Sun, Y. Wang, X. Ren, B. Du, D. Wu and Q. Wei, *Biosens. Bioelectron.*, 2017, **96**, 239–245.
6 X. Yu, B. Munge, V. Patel, G. Jensen, A. Bhirde, J. D. Gong, S. N. Kim, J. Gillespie, J. S. Gutkind, F. Papadimitrakopoulos and J. F. Rusling, *J. Am. Chem. Soc.*, 2006, **128**, 11199–11205.
7 V. Palomo, S. A. Díaz, M. H. Stewart, K. Susumu, I. L. Medintz and P. E. Dawson, *ACS Nano*, 2016, **10**, 6090–6099.
8 D. Mendez-Gonzalez, M. Laurenti, A. Latorre, A. Somoza, A. Vazquez, A. I. Negredo, E. López-Cabarcos, O. G. Calderón, S. Melle and J. Rubio-Retama, *ACS Appl. Mater. Interfaces*, 2017, **9**, 12272–12281.
9 F. Ghasemi, M. R. Hormozi-Nezhad and M. Mahmoudi, *Nanoscale*, 2018, **10**, 6361–6368.
10 P. Moitra, M. Alafeef, K. Dighe, M. B. Frieman and D. Pan, *ACS Nano*, 2020, **14**, 7617–7627.
11 B. D. Malhotra and M. A. Ali, in *Nanomaterials for Biosensors*, ed. B. D. Malhotra and M. A. Ali, William Andrew Publishing, 2018, pp. 1–74.
12 W. Zhou, K. Hu, S. Kwee, L. Tang, Z. Wang, J. Xia and X. Li, *Anal. Chem.*, 2020, **92**, 2739–2747.
13 T. A. P. Rocha-Santos, *TrAC, Trends Anal. Chem.*, 2014, **62**, 28–36.
14 L. Gloag, M. Mehdipour, D. Chen, R. D. Tilley and J. J. Gooding, *Adv. Mater.*, 2019, **31**, 1904385.
15 D. Sim, M. C. Brothers, J. M. Slocik, A. E. Islam, B. Maruyama, C. C. Grigsby, R. R. Naik and S. S. Kim, *Adv. Sci.*, 2022, **9**, 2104426.
16 M. Ouyang, D. Tu, L. Tong, M. Sarwar, A. Bhimaraj, C. Li, G. L. Coté and D. Di Carlo, *Biosens. Bioelectron.*, 2021, **171**, 112621.
17 F. Gambinossi, S. E. Mylon and J. K. Ferri, *Adv. Colloid Interface Sci.*, 2015, **222**, 332–349.
18 G. Fu, S. T. Sanjay, W. Zhou, R. A. Brekken, R. A. Kirken and X. Li, *Anal. Chem.*, 2018, **90**, 5930–5937.
19 A. Latorre, C. Posch, Y. Garcimartín, S. Ortiz-Urda and Á. Somoza, *Chem. Commun.*, 2014, **50**, 3018–3020.
20 M. Donolato, P. Antunes, R. S. Bejhed, T. Z. Gómez de la Torre, F. W. Østerberg, M. Strömberg, M. Nilsson, M. Strømme, P. Svedlindh, M. F. Hansen and P. Vavassori, *Anal. Chem.*, 2015, **87**, 1622–1629.
21 A. Moyano, M. Salvador, J. C. Martínez-García, V. Socoliuc, L. Vékás, D. Peddis, M. A. Alvarez, M. Fernández, M. Rivas and M. C. Blanco-López, *Anal. Bioanal. Chem.*, 2019, **411**, 6615–6624.
22 J. M. Perez, F. J. Simeone, Y. Saeki, L. Josephson and R. Weissleder, *J. Am. Chem. Soc.*, 2003, **125**, 10192–10193.
23 Z. Ma, J. Mohapatra, K. Wei, J. P. Liu and S. Sun, *Chem. Rev.*, 2023, **123**(7), 3904–3943.
24 G. Mistlberger, K. Koren, E. Scheucher, D. Aigner, S. M. Borisov, A. Zankel, P. Pölt and I. Klimant, *Adv. Funct. Mater.*, 2010, **20**, 1842–1851.
25 A. Fornara, P. Johansson, K. Petersson, S. Gustafsson, J. Qin, E. Olsson, D. Ilver, A. Krozer, M. Muhammed and C. Johansson, *Nano Lett.*, 2008, **8**, 3423–3428.
26 S. Gandhi, H. Arami and K. M. Krishnan, *Nano Lett.*, 2016, **16**, 3668–3674.
27 S. Schrittwieser, F. Ludwig, J. Dieckhoff, K. Soulantica, G. Viau, L.-M. Lacroix, S. M. Lentijo, R. Boubekri, J. Maynadié, A. Huetten, H. Brueckl and J. Schotter, *ACS Nano*, 2012, **6**, 791–801.

28 J. Zhong, E. L. Rösch, T. Viereck, M. Schilling and F. Ludwig, *ACS Sens.*, 2021, **6**, 976–984.
29 T. Mizoguchi, A. Kandori, R. Kawabata, K. Ogata, T. Hato, A. Tsukamoto, S. Adachi, K. Tanabe, S. Tanaka, K. Tsukada and K. Enpuku, *IEEE Trans. Appl. Supercond.*, 2016, **26**, 1–4.
30 A. R. Chalifour, J. C. Davidson, N. R. Anderson, T. M. Crawford and K. L. Livesey, *Phys. Rev. B*, 2021, **104**, 094433.
31 C. Min, H. Shao, M. Liong, T.-J. Yoon, R. Weissleder and H. Lee, *ACS Nano*, 2012, **6**, 6821–6828.
32 M. Varshney and K. Mallikarjunan, *Resour.: Eng. Technol. Sustain. World*, 2009, **16**, 18–21.
33 E. Hemmer, A. Benayas, F. Légaré and F. Vetrone, *Nanoscale Horiz.*, 2016, **1**, 168–184.
34 F.-X. Schmid, in *Encyclopedia of Life Sciences*, 2001.
35 S. Hildebrand, N. Löwa, H. Paysen, R. M. Fratila, L. Reverte-Salisa, T. Trakoolwilaiwan, Z. Niu, G. Kasparis, S. F. Preuss, O. Kosch, J. M. de la Fuente, N. T. K. Thanh, F. Wiekhorst and A. Pfeifer, *ACS Nano*, 2021, **15**, 434–446.
36 M. Meister, *eLife*, 2016, **5**, e17210.
37 K. Wu, D. Tonini, S. Liang, R. Saha, V. K. Chugh and J.-P. Wang, *ACS Appl. Mater. Interfaces*, 2022, **14**, 9945–9969.
38 P. Palacios-Alonso, E. Sanz-de Diego, R. P. Peláez, A. L. Cortajarena, F. J. Teran and R. Delgado-Buscalioni, *Soft Matter*, 2023, **19**, 8929–8944.
39 J. G. Ovejero, D. Cabrera, J. Carrey, T. Valdivielso, G. Salas and F. J. Teran, *Phys. Chem. Chem. Phys.*, 2016, **18**, 10954–10963.
40 L. C. Branquinho, M. S. Carrião, A. S. Costa, N. Zufelato, M. H. Sousa, R. Miotto, R. Ivkov and A. F. Bakuzis, *Sci. Rep.*, 2013, **3**, 2887.
41 D. Cabrera, A. Lak, T. Yoshida, M. E. Materia, D. Ortega, F. Ludwig, P. Guardia, A. Sathya, T. Pellegrino and F. J. Teran, *Nanoscale*, 2017, **9**, 5094–5101.
42 N. Telling, in *Nanomaterials for Magnetic and Optical Hyperthermia Applications*, Elsevier, 2019, pp. 173–197.
43 D. Cabrera, A. Coene, J. Leliaert, E. J. Artés-Ibáñez, L. Dupré, N. D. Telling and F. J. Teran, *ACS Nano*, 2018, **12**, 2741–2752.
44 S. Ota, R. Kitaguchi, R. Takeda, T. Yamada and Y. Takemura, *Nanomaterials*, 2016, **6**(9), 170.
45 A. Aires, D. Cabrera, E. Artés, A. Cortajarena and F. Teran, *Method for detection of an analyte*, 2019.
46 M. E. Jackrel, R. Valverde and L. Regan, *Protein Sci.*, 2009, **18**(4), 762–774.
47 R. P. Ilagan, E. Rhoades, D. F. Gruber, H.-T. Kao, V. A. Pieribone and L. Regan, *FEBS J.*, 2010, **277**, 1967–1978.
48 D. Serantes, K. Simeonidis, M. Angelakeris, O. Chubykalo-Fesenko, M. Marciello, M. del P. Morales, D. Baldomir and C. Martinez-Boubeta, *J. Phys. Chem. C*, 2014, **118**, 5927–5934.
49 M. V. Zyuzin, M. Cassani, M. J. Barthel, H. Gavilan, N. Silvestri, A. Escudero, A. Scarpellini, F. Lucchesi, F. J. Teran, W. J. Parak and T. Pellegrino, *ACS Appl. Mater. Interfaces*, 2019, **11**, 41957–41971.
50 E. Ximendes, R. Marin, Y. Shen, D. Ruiz, D. Gómez-Cerezo, P. Rodríguez-Sevilla, J. Lifante, P. X. Viveros-Méndez, F. Gámez, D. García-Soriano, G. Salas, C. Zalbidea, A. Espinosa, A. Benayas, N. García-Carrillo, L. Cussó, M. Desco, F. J. Teran, B. H. Juárez and D. Jaque, *Adv. Mater.*, 2021, **33**, 2100077.
51 D. Cabrera, T. Yoshida, T. Rincón-Domínguez, J. L. F. Cuñado, G. Salas, A. Bollero, M. del P. Morales, J. Camarero and F. J. Teran, *Nanoscale*, 2022, **14**, 8789–8796.
52 F. L. Durhuus, L. H. Wandall, M. H. Boisen, M. Kure, M. Beleggia and C. Frandsen, *Nanoscale*, 2021, **13**, 1970–1981.
53 J. Dieckhoff, D. Eberbeck, M. Schilling and F. Ludwig, *J. Appl. Phys.*, 2016, **119**, 043903.
54 D. Niculaes, A. Lak, G. C. Anyfantis, S. Marras, O. Laslett, S. K. Avugadda, M. Cassani, D. Serantes, O. Hovorka, R. Chantrell and T. Pellegrino, *ACS Nano*, 2017, **11**, 12121–12133.
55 C. Martinez-Boubeta, K. Simeonidis, D. Serantes, I. Conde-Leborán, I. Kazakis, G. Stefanou, L. Peña, R. Galceran, L. Balcells, C. Monty, D. Baldomir, M. Mitrakas and M. Angelakeris, *Adv. Funct. Mater.*, 2012, **22**, 3737–3744.
56 A. Sathya, P. Guardia, R. Brescia, N. Silvestri, G. Pugliese, S. Nitti, L. Manna and T. Pellegrino, *Chem. Mater.*, 2016, **28**, 1769–1780.
57 R. Di Corato, A. Quarta, P. Piacenza, A. Ragusa, A. Figuerola, R. Buonsanti, R. Cingolani, L. Manna and T. Pellegrino, *J. Mater. Chem.*, 2008, **18**, 1991.
58 *Far-Field Optical Nanoscopy*, ed. P. Tinnefeld, C. Eggeling and S. W. Hell, Springer Berlin Heidelberg, Berlin, Heidelberg, 2015, vol. 14.
59 M. L. Martin-Fernandez, C. J. Tynan and S. E. D. Webb, *J. Microsc.*, 2013, **252**, 16–22.
60 S. Wolter, A. Löschberger, T. Holm, S. Aufmkolk, M.-C. Dabauvalle, S. van de Linde and M. Sauer, *Nat. Methods*, 2012, **9**, 1040–1041.
61 S. E. D. Webb, M. Hirsch, S. R. Needham, B. C. Coles, K. M. Scherer, S. K. Roberts, L. C. Zanetti-Domingues, C. J. Tynan, M. L. Martin-Fernandez and D. J. Rolfe, *Super-Resolut. Light Microsc.*, 2015, **88**, 76–80.
62 S. R. Needham, M. Hirsch, D. J. Rolfe, D. T. Clarke, L. C. Zanetti-Domingues, R. Wareham and M. L. Martin-Fernandez, *PLoS One*, 2013, **8**, 13.
63 R. P. Peláez, *Universally Adaptable Multiscale Molecular Dynamics*, **https://github.com/RaulPPelaez/UAMMD**.
64 R. P. Peláez, Complex fluids in the Gpu era. Algorithms and simulations, *UAM. Departamento de Física Teórica de la Materia Condensada*, 2022.
65 A. Vázquez-Quesada, F. Balboa Usabiaga and R. Delgado-Buscalioni, *J. Chem. Phys.*, 2014, **141**, 204102.
66 S. Delong, F. Balboa Usabiaga, R. Delgado-Buscalioni, B. E. Griffith and A. Donev, *J. Chem. Phys.*, 2014, **140**, 134110.
67 J. Leliaert, A. Vansteenkiste, A. Coene, L. Dupré and B. Van Waeyenberge, *Med. Biol. Eng. Comput.*, 2015, **53**, 309–317.

68 W. F. Brown, *Phys. Rev.*, 1963, **130**, 1677–1686.
69 S. G. Sherman and N. M. Wereley, *IEEE Trans. Magn.*, 2013, **49**, 3430–3433.
70 W. Liu, M. Zhou and L. Kong, *Meas. Sci. Technol.*, 2009, **20**, 125802.
71 R. M. Ferguson, K. R. Minard, A. P. Khandhar and K. M. Krishnan, *Med. Phys.*, 2011, **38**, 1619–1626.
72 S. W. Davis, W. McCausland, H. C. McGahagan, C. T. Tanaka and M. Widom, *Phys. Rev. E: Stat. Phys., Plasmas, Fluids, Relat. Interdiscip. Top.*, 1999, **59**, 2424–2428.
73 J. P. Huang, Z. W. Wang and C. Holm, *Phys. Rev. E: Stat., Nonlinear, Soft Matter Phys.*, 2005, **71**, 061203.
74 Z. Wang, C. Holm and H. W. Müller, *Phys. Rev. E: Stat., Nonlinear, Soft Matter Phys.*, 2002, **66**, 021405.